AIAA JOURNAL
Vol. 42, No. 3, March 2004

Turbulent Inflow Conditions for Large-Eddy Simulation of Compressible Wall-Bounded Flows

Pierre Sagaut*
Université Pierre et Marie Curie, 5 Paris CEDEX, France
and
Eric Garnier,† Eric Tromeur,‡ Lionel Larchevêque,§ and Emmanuel Labourasse§
ONERA, 92322 Châtillon CEDEX, France

The issue of turbulent inflow conditions for large-eddy simulation (LES) is addressed through three representative examples recently treated at ONERA. First, the performance of an extension to compressible flows of the rescaling method of Lund et al. (Lund, T. S., Wu, X., and Squire, K. D., "Generation of Turbulent Inflow Data for Spatially-Developing Boundary Layer Simulations," *Journal of Computational Physics*, Vol. 140, No. 2, 1998, pp. 233–258) is assessed. The second example, the flow above a deep cavity shows that the imposition of turbulent fluctuations has nearly no influence on the accuracy of the simulation on this acoustically driven flow. The third case demonstrates that particular attention must be paid to the response of the inflow condition to acoustic perturbations when local hybrid Reynolds-averaged Navier–Stokes/LES approaches are considered.

I. Introduction

THIS paper presents the work undertaken at ONERA dealing with the important issue of generating realistic turbulent inflow conditions for direct numerical and large-eddy simulations (DNS/LES) (see Ref. 1 for a survey).

In most applications, the state of the inflow turbulence can have a substantial influence on the results of unsteady simulations, and particular attention must be paid to this issue because it is usually not possible to use these computationally expensive methods to treat the whole extension of the considered application. For example, in a shock/turbulent boundary-layer interaction it is currently impossible to compute both the natural transition of the boundary layer and the interaction zone.

The choice of the method to specify this inflow condition is problem dependent; the following approaches can be considered:

1) Add to the mean velocity profile realistic perturbations computed with parabolic stability equations in their early nonlinear regime so that the transition occurs quickly downstream the inflow plane. This approach is limited to low-Reynolds-number computations.

2) Use experimental data treated by linear stochastic estimation, which can be used to reconstruct two-points correlations of the velocity field (see paper by Druault et al.[2]).

3) Decompose a turbulent signal coming from experimental or numerical data on a proper-orthogonal-decomposition basis, and use this highly compressed signal as inflow condition.

4) Superimpose a white noise to the mean velocity profile. This method necessitates the use of large computational domain to allow the regeneration of a turbulent flow.

5) Generate data from another precursor simulation.

6) Dedicate a part of the computational domain to the use of a recycling method.

If the two latter methods are used to generate realistic conditions for a boundary layer, the most promising way is to choose the method of rescaling proposed by Lund et al.[3] to prevent the thickening of the boundary layer. Possible extensions of this method to compressible flow are numerous, and part of the work presented in this paper is dedicated to this issue. Nevertheless, the use of this method can be hard to implement, and it is interesting to assess cases for which a white noise superimposed on a mean profile can be sufficient. Furthermore, in some cases it is not easy to determine if the behavior of the inflow condition with respect to acoustic perturbation is more important than the realism of the velocity perturbations.

This paper is split into three parts. First the Lund et al.[3] method is considered, and three extensions of this method for compressible flows found in the literature are presented. The limits of these three approaches for long time integration are demonstrated on the case of a spatially developing supersonic boundary layer, and a way to really fix boundary layer scales is assessed. In a second part, the influence of the inflow conditions on a LES of a flow above a deep cavity is characterized. The third part addresses the issue of inflow conditions for a zonal hybrid Reynolds-averaged Navier–Stokes (RANS)/LES approach [namely, an extension of the nonlinear disturbance equations (NLDE) method] applied to the computation of a low-pressure turbine blade. In this case, the turbulent fluctuations are only computed locally, and the inflow condition is located in the transitional part of the boundary layer. This three test cases allow us to analyze the need for inflow conditions for an attached flow, for an acoustically driven flow and for a transitional flow.

II. Rescaling Methods

A. Model of Lund et al.

For incompressible flows, the turbulent inflow conditions can be generated by a rescaling technique proposed by Lund et al.[3] The main idea of the rescaling-recycling method is to use rescaled data taken at a downstream station as inflow data.

The idea is to decompose each flowfield component into a mean and a fluctuating part and then apply the appropriate scaling law to each one separately. A variable $u_i(x, y, z, t)$ is decomposed as the sum of an average in the spanwise direction and in time $U_i(x, z)$

Presented as Paper 2003-0068 at the AIAA 41st Aerospace Sciences Meeting, Reno, NV, 6–9 January 2003; received 30 June 2003; revision received 24 September 2003; accepted for publication 23 October 2003.

*Professor, Laboratoire de Modélisation pour la Mécanique, Boite 162, 4 Place Jussieu 75252; also Consultant, Computational Fluid Dynamics and Aeroacoustics Department, ONERA, 92322 Châtillon CEDEX, France.

†Research Engineer, Applied Aerodynamic Department, B.P. 72, 29 av. de la Division Leclerc.

‡Ph.D. Student, Applied Aerodynamic Department, B.P. 72, 29 av. de la Division Leclerc.

§Ph.D. Student, Computational Fluid Dynamics and Aeroacoustics Department, B.P. 72, 29 av. de la Division Leclerc.

and an instantaneous fluctuating part $u_i'(x, y, z, t)$ according to

$$u_i'(x, y, z, t) = u_i(x, y, z, t) - U_i(x, z) \tag{1}$$

The index i is equal to 1, 2, and 3, and we denote the streamwise, spanwise, and wall-normal velocity components by u_1, u_2, and u_3, the corresponding coordinates being x, y, and z.

Then, in the rescaling method the velocity at the downstream station to be rescaled (index re) can be linked with that at the inlet (index in) via the relations presented here: for the inner region $U_{1,\text{in}}^{inner} = \beta U_{1,\text{re}}(z_{\text{in}}^+)$, $U_{2,\text{in}}^{inner} = 0$, $U_{3,\text{in}}^{inner} = U_{3,\text{re}}(z_{\text{in}}^+)$, and $(u_i')_{\text{in}}^{inner} = \beta(u_i')_{\text{re}}(y, z_{\text{in}}^+, t)$; and for the outer region $U_{1,\text{in}}^{outer} = \beta U_{1,\text{re}}(\eta_{\text{in}}) + (1-\beta)U_\infty$, $U_{2,\text{in}}^{outer} = 0$, $U_{3,\text{in}}^{outer} = U_{3,\text{re}}(\eta_{\text{in}})$, and $(u_i')_{\text{in}}^{outer} = \beta(u_i')_{\text{re}}(y, \eta_{\text{in}}, t)$. The mean and fluctuating velocities are decomposed into inner and outer variables.

The rescaling factor $\beta = u_{\tau,\text{in}}/u_{\tau,\text{re}}$ is the ratio of friction velocities respectively at the inlet station and at the recycled station. Notice that $z_{\text{in}}^+ = z u_{\tau,\text{in}}/\nu$ and $\eta_{\text{in}} = z/\delta_{\text{in}}$ are inner and outer coordinates at the inlet station.

Complete velocity profiles valid over the entire inflow boundary layer are obtained by a weighted average of inner and outer profiles:

$$(u_i)_{\text{in}} = \left[(U_i)_{\text{in}}^{inner} + (u_i')_{\text{in}}^{inner}\right][1 - W(\eta_{\text{in}})] + \left[(U_i)_{\text{in}}^{outer} + (u_i')_{\text{in}}^{outer}\right]W(\eta_{\text{in}})$$

The weighting function W is defined as

$$W(\eta) = \frac{1}{2}\left\{1 + \tanh\left[\frac{\alpha(\eta - b)}{(1-2b)\eta + b}\right] \Big/ \tanh(\alpha)\right\} \tag{2}$$

where $\alpha = 4$ and $b = 0.2$.

The rescaling operation requires the knowledge of the skin-friction velocity u_τ and the boundary-layer thickness δ, both at the rescaling station and at the inlet. These quantities can be determined easily from the mean velocity profile at the recycled station, but they must be specified at the inlet. Lund et al.[3] propose to fix δ at the inlet, whereas u_τ is evaluated through the relation

$$u_{\tau,\text{in}} = u_{\tau,\text{re}}\left(\frac{\theta_{\text{re}}}{\theta_{\text{in}}}\right)^{1/[2(n-1)]} \tag{3}$$

where θ is the incompressible momentum thickness and the exponent n is set to 5.

Table 1 Summary of rescaling methods for compressible flow

Reference	U	T	ρ	β
5	S.1	S.3	S.4	$\left(\frac{\delta_{\text{re}}}{\delta_{\text{in}}}\right)^{\frac{1}{8}}$
4	S.2	S.3	No	$\left(\frac{\delta_{\text{re}}}{\delta_{\text{in}}}\right)^{\frac{1}{10}}$
6	S.1	S.5	No	$\sqrt{\frac{\rho_{(wall)_{\text{re}}}}{\rho_{(wall)_{\text{in}}}}}\left(\frac{\delta_{1_{\text{re}}}}{\delta_{1_{\text{in}}}}\right)^{\frac{1}{8}}$

B. Spatially Developing Simulation for Compressible Flows

For compressible flows, extensions of the technique by Lund et al.[3] have been presented in Refs. 4–6. For this type of flow, the problem is more complicated because a rescaling law for two thermodynamic variables must be defined.

The rescaling methods for compressible flow published in the literature are summarized in Table 1.

According to Urbin and Knight[4] and Schröder et al.,[6] the pressure is assumed to be constant, and a rescaling for ρ is not to be specified.

S.1 denotes the same rescaling strategy as Lund et al.[3] for the mean streamwise velocity, whereas S.2 uses the Van Driest transformation of the velocity U_{VD} for the rescaling of this quantity:

$$U_{\text{VD,in}}^{inner} = \beta U_{\text{VD,re}}\left(z_{\text{in}}^+\right)$$

$$U_{\text{VD,in}}^{outer} = \beta U_{\text{VD,re}}(\eta_{\text{in}}) + (1-\beta)U_{\text{VD}}^{\infty}$$

where

$$U_{\text{VD}} = \frac{U_\infty}{A}\sin^{-1}\left(A\frac{U}{U_\infty}\right)$$

with

$$A = \sqrt{\frac{[(\gamma-1)/2]M_\infty^2 Pr_{\text{tm}}}{1 + [(\gamma-1)/2]M_\infty^2 Pr_{\text{tm}}}}$$

$Pr_{\text{tm}} = 0.89$ is the mean turbulent Prandtl number.

The rescaling of the wall-normal velocity and fluctuating velocities is the same as the one of Lund et al.[3] for all authors.

Moreover, to obtain β Urbin and Knight[4] impose the ratio $\delta_{\text{re}}/\delta_{\text{in}}$ according the following classical law:

$$\frac{\delta_{\text{re}}}{\delta_{\text{in}}} = \left[1 + \left(\frac{x_{\text{re}} - x_{\text{in}}}{\delta_{\text{in}}}\right)0.27^{\frac{6}{5}}Re_{\delta_{\text{in}}}^{-\frac{1}{5}}\right]^{\frac{5}{6}}$$

where $Re_{\delta_{\text{in}}}$ is the Reynolds number based on the inflow boundary-layer thickness.

Rescaling strategies S.3, S.4, and S.5 are detailed in Table 2, where $C_1 = (1+A)(1-\beta^2)$, $C_2 = 2A\beta(1-\beta)$, and $C_3 = (1-\beta)[1+\beta+2A\beta]$.

III. Evaluation of These Methods for Long Time Integration

First, we have performed an evaluation of the three methods just described on the case of a canonical supersonic boundary layer developing on a plane plate at Mach number 2.3. This test case has been studied experimentally by the team of J. P. Dussauge at the Institut de Recherche sur les Phénomènes hors Equilibre. The results using laser Doppler anemometry (LDA) can be found in the Ph.D. dissertation of Deleuze[7] and the results obtained with hot-wire anemometry (HWA) are available in the Laurent's Ph.D. dissertation.[8]

Table 2 Rescaling strategies for density and temperature

Method	Inner region	Outer region
S.3	$T_{\text{in}}^{inner} = T_{\text{re}}\left(z_{\text{in}}^+\right)$	$T_{\text{in}}^{outer} = T_{\text{re}}(\eta_{\text{in}})$
	$T_{\text{in}}^{'inner} = T_{\text{re}}'(y, z_{\text{in}}^+, t)$	$T_{\text{in}}^{'outer} = T_{\text{re}}'(y, \eta_{\text{in}}, t)$
S.4	$\rho_{\text{in}}^{inner} = \rho_{\text{re}}\left(z_{\text{in}}^+\right)$	$\rho_{\text{in}}^{outer} = \rho_{\text{re}}(\eta_{\text{in}})$
	$\rho_{\text{in}}^{'inner} = \rho_{\text{re}}'(y, z_{\text{in}}^+, t)$	$\rho_{\text{in}}^{'outer} = \rho_{\text{re}}'(y, \eta_{\text{in}}, t)$
S.5	$T_{\text{in}}^{inner} = \beta^2 T_{\text{re}}(z_{\text{in}}^+) + C_1 T_e$	$T_{\text{in}}^{outer} = \beta^2 T_{\text{re}}(\eta_{\text{in}}) - C_2\frac{U_{\text{re}}(\eta_{\text{in}})}{U_e}T_e + C_3 T_e$
	$T_{\text{in}}^{'inner} = \beta^2 T_{\text{re}}'(y, z_{\text{in}}^+, t)$	$T_{\text{in}}^{'outer} = \beta^2 T_{\text{re}}'(y, \eta_{\text{in}}, t) - C_2\frac{u_{\text{re}}'(y, \eta_{\text{in}}, t)}{U_e}T_e$

The temperature T_e outside of the boundary layer is 144.6 K, the density ρ_e is equal to 9.66 10^{-2} kg/m^3, and the velocity value U_e is 557 m/s. The reference length chosen in those computations is the measured displacement length δ_1, which is equal to 3.535 mm. This length is defined as

$$\delta_1 = \int_0^\infty \left(1 - \frac{\rho u}{\rho_e U_e}\right) \mathrm{d}z \tag{4}$$

The Reynolds number $Re(\delta_1)$ based on the displacement length U_e, ρ_e, and $\mu(T_e)$ is equal to 19132. The boundary-layer height δ is 11 mm.

A. Computational Parameters

The number of grid points in each direction are $159 \times 63 \times 115$, and the size of the computational domain is $10.7\delta \times 1.4\delta \times 4.2\delta$. The size of the computational cells given in wall units are $\Delta_x^+ = 50$, $\Delta_y^+ = 18$, and $\Delta_z^+ = 1$ at the wall. We emphasize that these wall units are based on the experimentally measured friction velocity equal to 24.75 m/s.

The numerical method is fully described in Ref. 9. The algorithm is based on a fourth-order-accurate skew-symmetric discretization of the convective fluxes and a second-order-accurate centered scheme for the diffusive fluxes. The time integration is performed with a third-order-accurate Runge–Kutta scheme. The subgrid-scale model is the selective mixed-scale model presented in Ref. 10.

B. Results

The three methods presented above were run in a time equal to $105\delta/U_e$. Figures 1–3 display the time-averaged longitudinal evolution of δ and δ_1 at different times. One can expect that the inflow value of these two quantities remain constant in time and equal to its target value. Nevertheless, on long integration time one can clearly observe a divergence of these quantities from their target values. Using the method proposed in the Ref. 5, δ seems to converge toward the target value, but δ_1 is clearly underestimated. The method proposed by Urbin and Knight[4] underestimates δ by 12% and δ_1 diverges continuously to a too small value. Furthermore, the method proposed by Schröder et al.[6] is able to keep the target value of δ_1 but undergoes a drift in δ. From these results, we observe that it is not possible to fix both δ and δ_1. Note that δ_1 is also a function of the density profile.

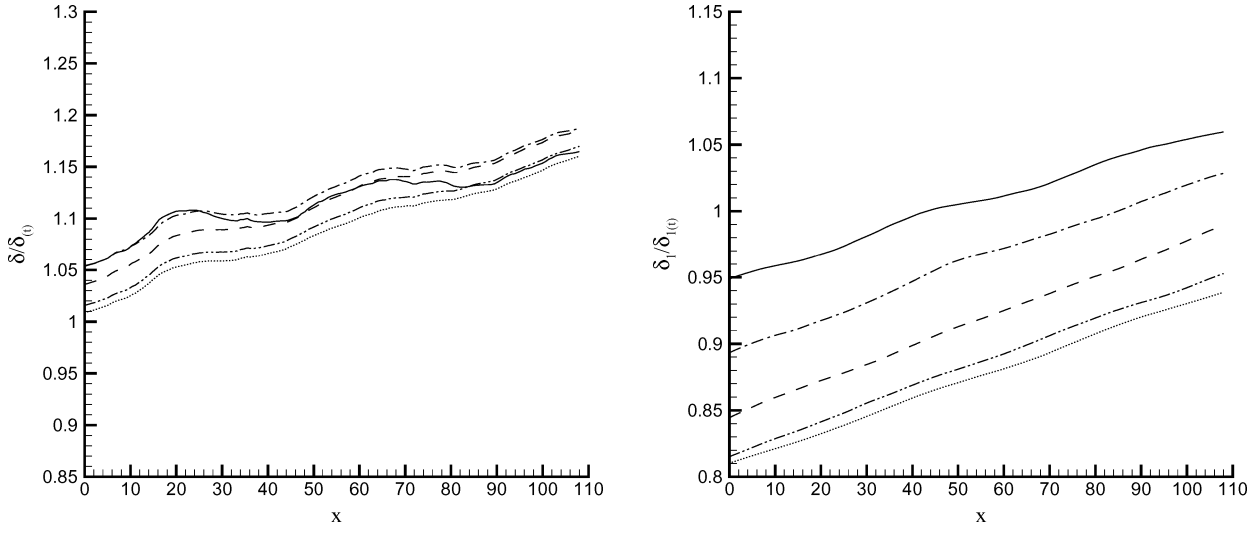

a) b)

Fig. 1 Longitudinal evolution of a) δ and b) δ_1 for different simulation times with the method proposed in Ref. 5: ——, $t = 47$; – · · –, $t = 63$; – – –, $t = 79$; – · · –, $t = 94$; and · · · ·, $t = 105$.

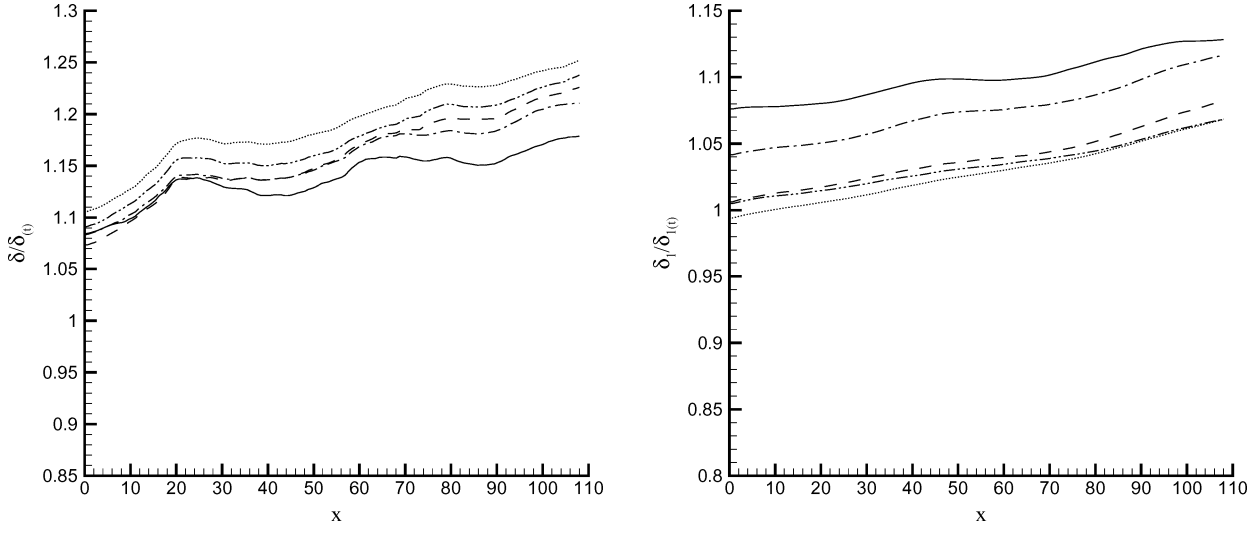

a) b)

Fig. 2 Longitudinal evolution of a) δ and b) δ_1 for different simulation times with the method proposed in Ref. 6: ——, $t = 47$; – · · –, $t = 63$; – – –, $t = 79$; – · · –, $t = 94$; and · · · ·, $t = 105$.

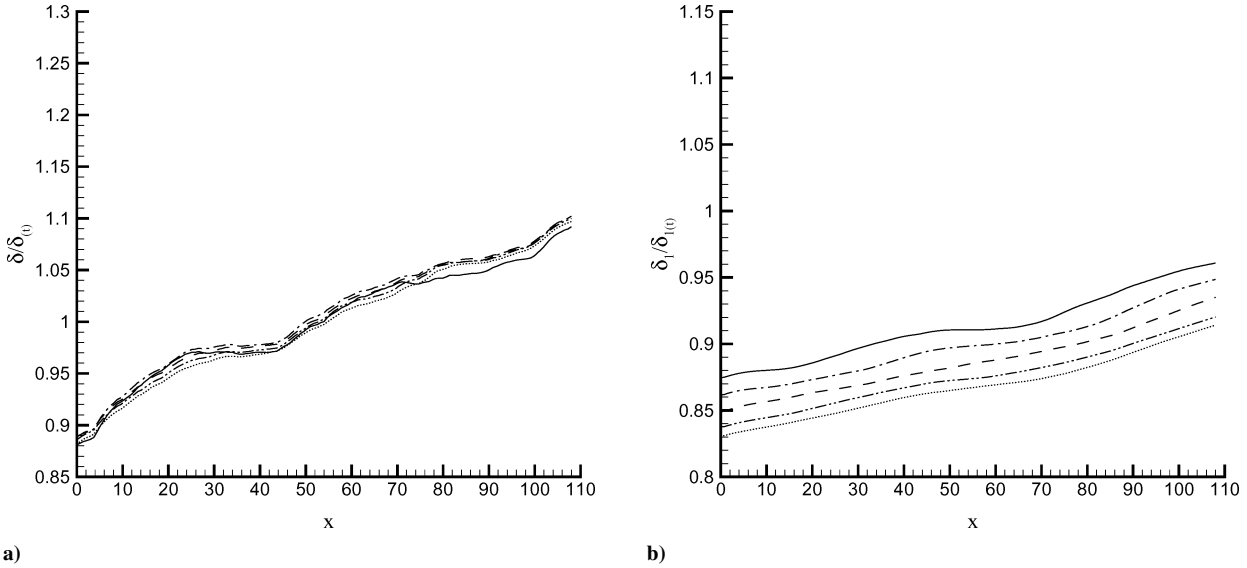

a) b)

Fig. 3 Longitudinal evolution of a) δ and b) δ_1 for different simulation times with the method proposed in Ref. 4: ——, $t = 47$; – · · –, $t = 63$; – – –, $t = 79$; – · – –, $t = 94$; and · · · ·, $t = 105$.

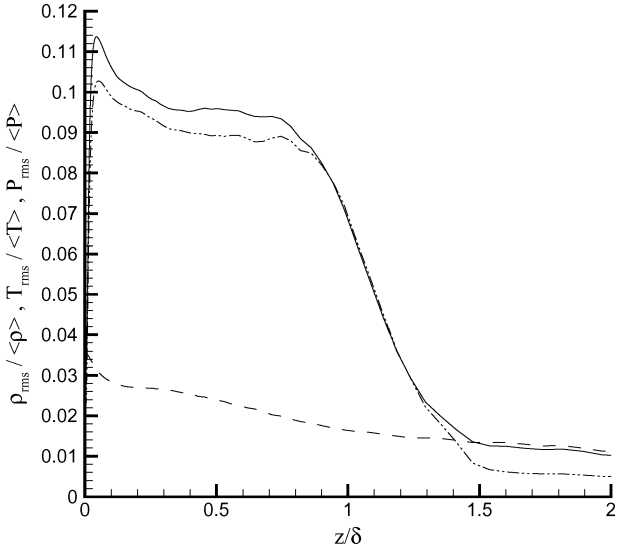

Fig. 4 Thermodynamic variables fluctuations profiles in the boundary layer: ——, $\rho_{rms}/\langle\rho\rangle$; – – –, $P_{rms}/\langle P\rangle$; and –·–·–, $T_{rms}/\langle T\rangle$.

IV. Way to Avoid Drift

To avoid this drift of the mean profile for all methods, it seems natural to fix this profile and to rescale only the fluctuations. Because the rescaling methods are restricted to canonical boundary layers, the mean profile is easy to fix from data coming from RANS computations, boundary-layer codes, experimental results, or LES used in the temporal approximation. In this work, the latter approach was chosen: a LES initialized with a perturbed laminar velocity profile was performed with strict periodicity conditions in the streamwise direction. This boundary layer becomes turbulent and unavoidably thickens continuously. If the target thickness for the inflow conditions of the spatial simulations is overshot, the Lund procedure is applied to rescale the boundary layer. The average (in streamwise and spanwise directions) of the obtained field is used as mean inflow condition for the spatial simulation, and the whole turbulent field (replicated in the streamwise and spanwise directions if necessary) is used as initial condition for this simulation.

Furthermore, one can see in Fig. 4 that the pressure fluctuations are not negligible when compared to temperature and density fluctuations. A very similar result can be found in Ref. 11. Because density and temperature are nearly anticorrelated in a compressible boundary layer, it is not sure that the rescaling of these two quantities as done in Refs. 4–6 uses all of the available information. For these two reasons, it was chosen to rescale both the temperature and the pressure. The chosen rescaling of the temperature is S.3, and the one for the pressure is the same as this of S.3 but with P instead of T.

Figure 5 displays the longitudinal evolution of δ and δ_1 for the proposed method. The time histories of these quantities are also reported, and one can notice that the drift has now nearly disappeared and that the target values are recovered within a 3% error. Note that integration time as long as $210\ \delta/U_e$ has been considered.

The Van Driest transformed mean velocity profiles obtained in the middle of the box are represented in Fig. 6. Both the computations and wind-tunnel experiments exhibit the expected logarithmic zone of equilibrium boundary layers. The experimental friction velocity is not measured but evaluated assuming the profile follows the classical law $\ell_n(z^+)/0.41 + 5.25$. This explains the perfect agreement of the experimental profile with this law. One can notice looking at the asymptotic value of U_{VD} that the friction velocity is underestimated by 10% with LES. This kind of underestimation is customary using LES and can also be found in Ref. 12 for a similar compressible boundary layer.

Following the work of Morkovin, longitudinal velocity fluctuations are multiplied by density and adimensionalized by friction velocity. This change of variable is used in Fig. 7. Discrepancies between LDA and HWA data are noticeable in particular near $z/\delta \sim 0.1$. Despite some experimental bias, former measurements at the same Mach number have led Eléna and Lacharme[13] to agree on the superiority of LDA measurements. For $z/\delta < 0.3$, LES results are located between those of both measurement techniques, whereas higher in the boundary layer numerical results are in nearly perfect agreement with LDA data.

Note that with mean profiles fixed the three aforementioned approaches give the same quantitative agreement that the method proposed here, which uses a pressure rescaling.

V. LES of a Flow past a Deep Cavity

A. Characteristics of the Computations

A configuration corresponding to the experiment of Forestier et al.[14] has been simulated. The Mach number in the inflow channel and the Reynolds number based on the length of the cavity are equal to 0.8 and 8.6×10^5, respectively. The incoming boundary layer has a momentum thickness upstream of the separation point equal to 0.648 mm. The length L and depth D of the cavity are equal to 50 and 120 mm, respectively. It results in a length to depth ratio of 0.42, and therefore the configuration belongs to the deep cavity

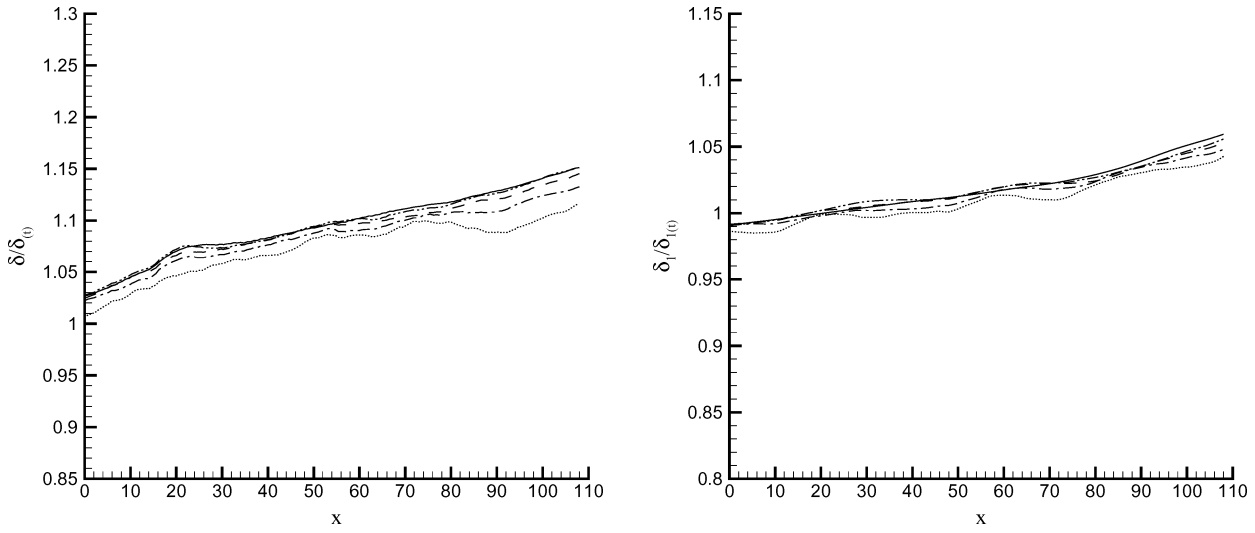

Fig. 5 Longitudinal evolution of a) δ and b) δ_1 for different simulation times with the method proposed method: · · · ·, $t = 73$; – · · –, $t = 84$; – – –, $t = 94$; – · · –, $t = 105$; and ——, $t = 210$.

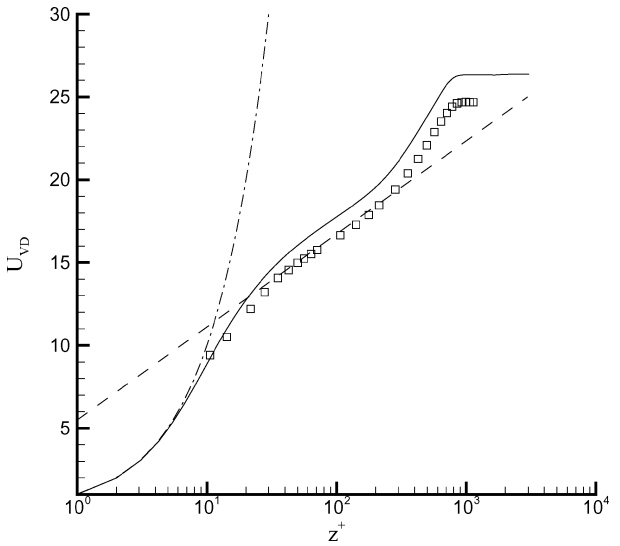

Fig. 6 Van Driest transformed inflow mean velocity: ——, LES; □, HWA; –·–·–, $U_{vd} = z^+$; – – –, $U_{vd} = \ell n(z^+)/0.41 + 5.25$.

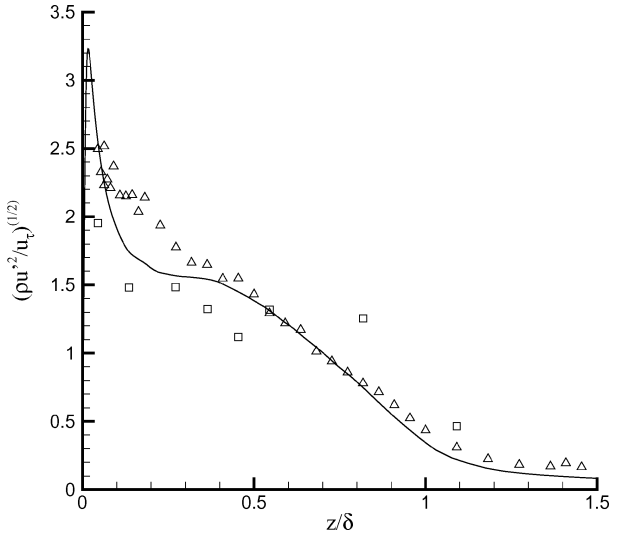

Fig. 7 Longitudinal velocity fluctuations profiles: ——, LES; □, HWA; and △, LDA.

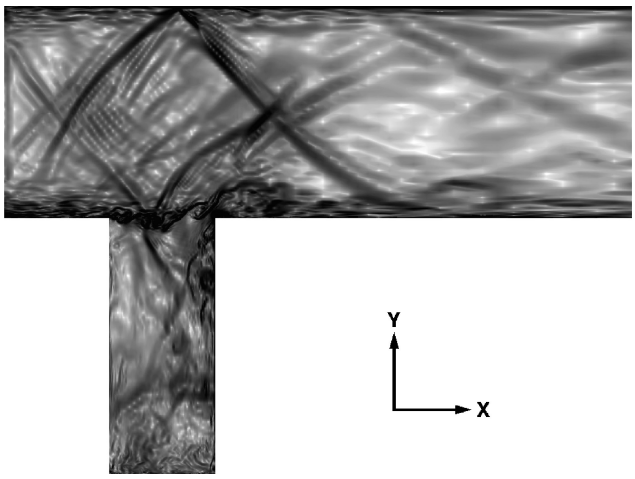

Fig. 8 Numerical schlieren view of the whole computational domain in the midspan x–y plane for F computation.

category. However, it resonates according to the flow-acoustic interaction (see Larchevêque et al.[15] for details).

The compressible filtered Navier–Stokes equations are closed using the selective mixed scales model[10] and the Prandtl analogy. The convective scheme is a second-order centered one, which possibly reverses to an upwind AUSM+(P)-like scheme according to a wiggle detector so as to prevent spurious oscillations (see Mary and Sagaut[16] for details). The time integration is carried out by means of a third-order compact Runge–Kutta scheme. To make the computation feasible, a two-layer law of the wall is used. Typical incoming channel boundary cells dimensions are $\Delta x^+ = 150$ (streamwise) and $\Delta y^+ = 120$ (normal to the wall).

The computational configuration mimics as close as possible the wind-tunnel geometry described in Ref. 14. Both lower and upper walls of the tunnel are taken into account. In the spanwise direction, periodicity conditions are used because the experimental measurements show that the flow is homogeneous along that direction. Details on the grid-convergence study and on the influence of the spanwise dimension upon computations results can be found in Ref. 15. For the present fully three-dimensional simulations, the span is set equal to the length of the cavity and is discretized with 50 cells. The resulting mesh has a total number of cells equal to 1.8 million, with one-half of these cells located into the cavity. Figure 8 provides an overlook of the computational domain in the midspan x–y plane.

Two computations have been carried out. Both of them use the experimental turbulent mean velocity profile as boundary condition, coupled with a Thomson nonreflective formulation. No velocity fluctuations are added in the first simulation, hereafter denoted NF. On the contrary, the second one, noted F, relies on velocity perturbations added at the inflow plane. These random perturbation values are obtained by means of a process, which is described in the next paragraph.

B. Turbulent Inflow Conditions

Because of the use of a spatial scheme, which includes a wiggle sensor, the inflow fluctuations have to be treated carefully in order to avoid an excessive damping. To neutralize the sensor in the wall-normal and transverse directions, the white-noise random values are filtered in each of these two directions using a $(\frac{1}{4}, \frac{1}{2}, \frac{1}{4})$ filter. The random fluctuation is then rescaled so that its variance σ^2 is equal to one.

To obtain a somehow similar neutralization in the streamwise direction, the filtered random values are time correlated using the following recursive relation:

$$V^{n+1} = \frac{\alpha \times V^n + (1-\alpha) \times U}{\sqrt{2 \times (\alpha^2 - \alpha) + 1}} \tag{5}$$

where V^n is the value of a random variable at the step n and U is a new space-filtered random value. The denominator helps to ensure that $\sigma^2(V) = 1$. This equation can be hold as a crude first-order discretization of a Langevin's equation. The parameter α is adjusted with regards to the inflow velocity and the time step so as to obtain reasonable spatial correlation length. For the present calculation, it has been set to 0.9. One can notice that because of the multiple summations of uniformly distributed random variables caused by the filtering and correlating process the distribution of the fluctuations is no longer uniform (white noise). It rather tends toward a Gaussian one (central limit theorem). Finally, the resulting random values are modulated according to spatial experimental u', v' and extrapolated w' fluctuating velocity profiles. One can notice that for low-Mach-number flows the white noise involved in this procedure should be made divergence free.

As it can be seen in Fig. 9, such a process is able to recover some kind of streamwise-oriented structures that can mimic streaks despite too great length ($\simeq 2000\, x^+$) and height (up to 400 y^+). This size is expected, considering the size of the mesh and the fact that a second-order-accurate numerical method is used. However a more appropriate behavior is progressively recovered further downstream. Also note that the spanwise structures observed slightly upstream of the cavity are generated under the influence of the mixing layer flow inside the cavity, as seen on the right part of the Fig. 9.

C. Analysis of the Results

Figure 10 shows the mean streamwise velocity profiles $0.1L$ before the upstream corner of the cavity. The two simulations lead to identical results in good concordance with the experimental measurements.

The fluctuating velocity profiles at the inflow and at the inflow ($x = -L$) and at $x = -0.1L$ are plotted in Figs. 11 and 12, respectively. The effect of the added fluctuations is clearly visible on the w' profiles, but not on the u' profiles. This has to be explained by the fact that u and v fluctuations are mainly caused by strong two-dimensional pressure waves traveling upstream the cavity (see Fig. 8). The main interest of the added fluctuations is therefore to provide the boundary layer with a more physical three-dimensional character. However, as it has been seen in Fig. 10 this three dimensionality does not affect the mean velocity profile. One can also notice that the procedure adopted to prevent dissipation of the fluctuation by the scheme is reasonably successful: inside the production region of the boundary layer the difference in w fluctuation levels between the F and NF cases remains almost constant along the inflow channel; as for the upper part of the layer, initial w fluctuations are damped by one-third to one-half.

The global quality of the simulation can be evaluated by looking at Figs. 13 and 14. Both NF and F simulations yield the same results in good agreement with the experimental measurements. More precisely, the three dimensionality of the boundary layer for F simulation has no impact on the flowfield inside the cavity. The intrinsic two-dimensional character of the primary Kelvin–Helmholtz instability is responsible for such a lack of sensitivity.

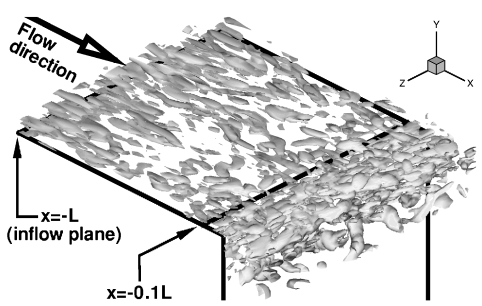

Fig. 9 Coherent structures in the inflow channel lower boundary layer (F computation). Structures are educed using the Q criterion.

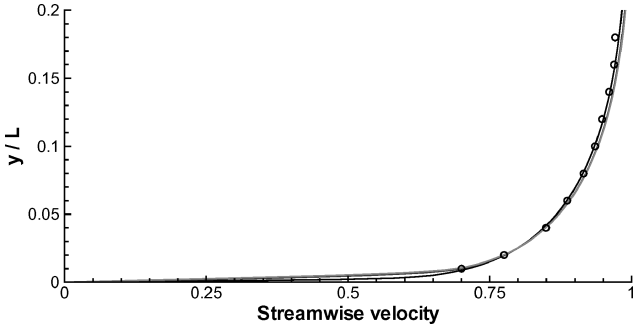

Fig. 10 Mean streamwise velocity profile at location $x = -0.1L$: ——, NF computation; – – –, F computation; and ○, experimental measurements.

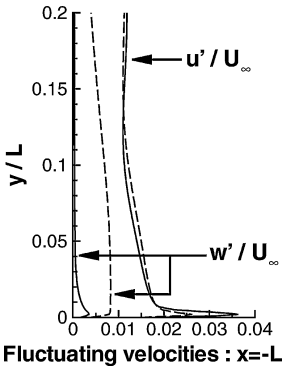

Fig. 11 Fluctuating velocity components at the inflow plane ($x = -L$): ——, NF computation; and – – –, F computation.

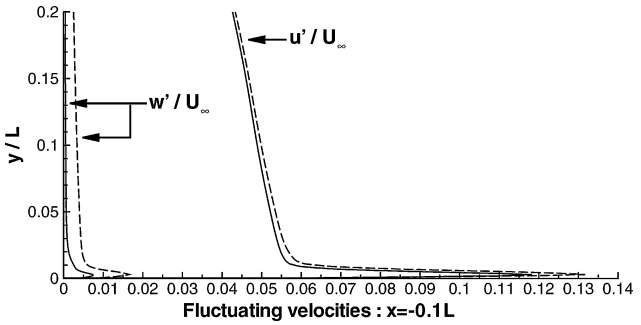

Fig. 12 Fluctuating velocity components at $x = -0.1L$: ——, NF computation; and – – –, F computation.

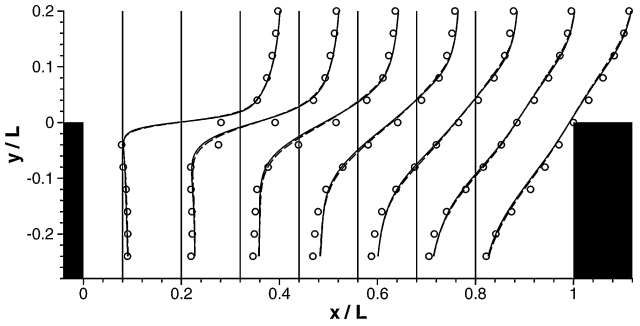

Fig. 13 Mean streamwise velocity profiles inside the mixing layer: ——, NF computation; – – –, F computation; and ○, experimental measurements.

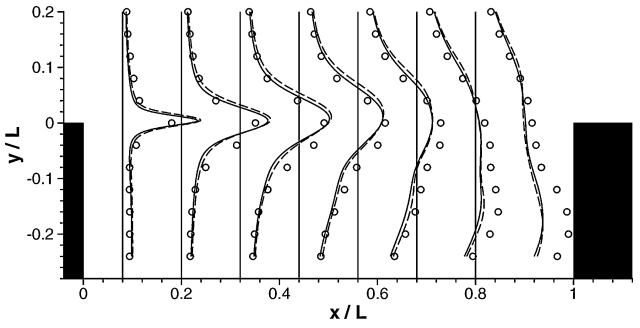

Fig. 14 Two-dimensional turbulent kinetic energy profiles inside the mixing layer: ——, NF computation; – – –, F computation; and ○, experimental measurements.

D. Learning from the Simulations

In these computations, the nature of the fluctuations of the inflow conditions appears to have no influence on the quality of the results. This can be explained by at least three facts:

1) The position of the separation point is imposed by the geometry of the configuration.

2) Pressure waves result in strong velocity fluctuations with level similar to or even higher than the "natural" ones observed in a canonic boundary layer.

3) The Kelvin–Helmholtz instability inside the mixing layer is rather sensitive to the mean boundary-layer profile than to the level of fluctuation. Indeed, the Kelvin–Helmholtz (K-H) instability in cavity flows initially acts as a noise amplifier, and therefore perturbation levels at its beginning should be of great importance. However, noting that K-H instability preferentially amplifies spanwise two-dimensional perturbations, three-dimensional boundary-layer structures have far less impact that the two-dimensional spanwise pressure-induced perturbations, even if they have lower magnitude than the boundary-layer ones.

The key of the success for such cavity simulations has rather to be found in the good description of the flow-acoustic resonance. Numerically speaking, this means that the mesh inside the cavity should have a good resolution in the vertical direction to adequately resolve the mixing-layer gradient and in the streamwise direction to correctly propagate the pressure waves. Because of the physics of the Kelvin–Helmholtz instability, a mean boundary-layer profile with the correct shape (momentum thickness) is also required.

Finally, because of its very low sensitivity to boundary-layer fluctuations the present cavity flow appears to be insufficient to completely analyze the inflow model just described. To obtain clear conclusions, the present method should be applied to other test cases for which turbulent fluctuation have a real impact on the flow development. Wall-bounded flows like curved boundary layer with separation or surface-mounted cube, as well as free flow like the one past a cylinder, could be considered. For free flows, results for the upper part of the boundary layer show that the model is promising. Also note that the model could be improved quite easily by cross correlating the velocity fluctuations prior to the filtering process.

VI. Application of a Hybrid RANS/LES Approach to a Low-Pressure Turbine Blade

A. Short Insight into NLDE

The method employed in this section can be seen as the generalization to viscous flows of the NLDE method proposed by Morris et al.[17] The principle of the method is to decompose the field u as a mean part (Reynolds average) and a fluctuating part as in Eq. (1). The mean part u_0 is then computed using a classical RANS modeling, whereas the calculation of the fluctuating part u' is achieved thanks to a LES-like simulation. The main originality of the method is that only the fluctuating part is computed during this second simulation, leading to the resolution of equations of the following form:

$$\frac{\partial u'}{\partial t} + \nabla \cdot F(\bar{u}) - \nabla \cdot F(u_0) = \tau^L - \tau^R \tag{6}$$

where - corresponds to the filtering in the LES way and τ^L and τ^R are respectively the classical subgrid scale tensor and the Reynolds tensor.

A full description of the method used in the present paper is given in Ref. 18.

B. Description of the Configuration

The NLDE method is employed to describe the aerodynamic field around the T106 low-pressure turbine blade. The complete LES calculation of this configuration can be found in Raverdy et al.[19] The NLDE is used to reconstruct the turbulent fluctuations both in the boundary layer and in the near wake. The gain with respect to the classical LES approach comes from the drastic reduction of the size of the computational domain. The mean flow is obtained carrying out a two-dimensional steady RANS computation on the same mesh and the same computational domain [in a $(x–z)$ plane] as the LES.[19] The Spalart–Allmaras model[20] is used in this case. Steady solution is obtained using a finite volume solver based on implicit time integration and a second-order-accurate upwind total-variation-diminishing scheme. The hybrid RANS/LES computations are performed in a subdomain containing the transition zone on the suction side of the blade, the trailing edge, and the near wake. Computational domains of LES, RANS, and hybrid RANS/LES computations are shown in Fig. 15.

RANS computation is carried out using the whole computational domain, which is divided in several subdomains. Shaded subdomains correspond to the computational domain used to reconstruct fluctuations using the NLDE approach.

Along the blade, the grid is defined such that $\Delta x^+ < 40$. The first grid point away from the wall is such that $\Delta z^+ \leq 1$. The number of points per $(x–z)$ plane is then reduced from 90,644 (LES, full computational domain) to 26,306 (NLDE method, restricted computational domain). The spanwise extent of the domain is 3.2% of the chord in both cases. Thirty points are used in this direction, yielding $\Delta y^+ < 10$. The resolution is such that the simulation is a quasi-DNS in the transition region and behaves like a well-resolved LES in turbulent regions. For the computation of the fluctuations,

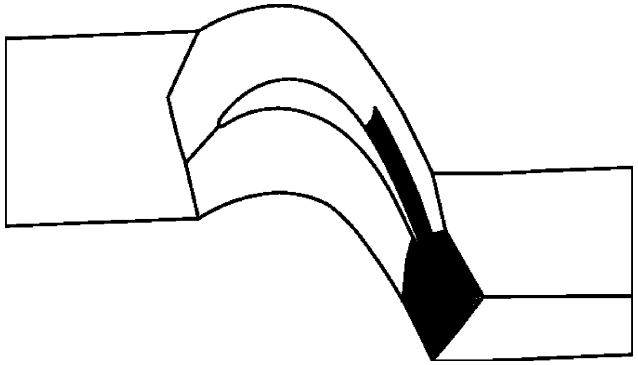

Fig. 15 Low-pressure turbine blade: RANS domains (white) and hybrid simulation domain (black).

the same numerical method as for the calculation of the deep cavity is used.

C. Characteristic Theory Applied to the NLDE Equations

Because of the reduction of the domain size, attention must be paid to the definition of the boundary conditions and particularly to the inflow ones. To deal with such short domain size, a nonreflecting time-dependent boundary condition for the fluctuation is derived according to the characteristic theory (see Ref. 21 for a review of this theory).

In the nonconservative form, the Navier–Stokes equation can be written:

$$\frac{\partial V}{\partial t} + A\frac{\partial V}{\partial x} + B\frac{\partial V}{\partial y} + C\frac{\partial V}{\partial z} = VIS \tag{7}$$

where $V = (\rho, u, v, w, p)^T$ is the primitive variable field; *VIS* accounts for the viscosity and subgrid scales terms; and A, B, and C are the classical convection matrices.

V can be divided in three parts according to the NLDE method:

$$V = V^0 + V' + V^{\mathrm{SGS}} \tag{8}$$

The first part, $V^0 = (\rho_0, u_0, v_0, w_0, p_0)^T$, deals with the statistically mean field, and the second part is connected with the fluctuating field, $V' = (\rho', u', v', w', p')^T$.

As in all of the other works dealing with the subject, the contribution of the subgrid scale term V^{SGS} is neglected.

This leads to the following equation for the fluctuating field:

$$\frac{\partial V'}{\partial t} + A\frac{\partial V'}{\partial x} + B\frac{\partial V'}{\partial y} + C\frac{\partial V'}{\partial z} = VIS'$$
$$-\left(\frac{\partial V^0}{\partial t} + A\frac{\partial V^0}{\partial x} + B\frac{\partial V^0}{\partial y} + C\frac{\partial V^0}{\partial z} - VIS_0\right) \tag{9}$$

where VIS' and VIS_0 account respectively for the fluctuating and mean part of the viscosity terms. By analogy with the extension of the characteristic theory to the viscous flows (for instance, see Ref. 22), only the terms of convection of the fluctuations are now considered, which leads to neglect the right-hand side of Eq. (9).

The resulting equation is the following one:

$$\frac{\partial V'}{\partial t} + A\frac{\partial V'}{\partial x} + B\frac{\partial V'}{\partial y} + C\frac{\partial V'}{\partial z} = 0 \tag{10}$$

Classically, the matrix $E = An_x + Bn_y + Cn_z$ [where $n = (n_x, n_y, n_z)^T$ is the vector normal to the considered boundary] has now to be diagonalized in order to set conditions on the characteristic variables of the equation. We can then write

$$\Lambda = LEL^{-1} = \mathrm{diag}(\lambda^1, \lambda^2, \lambda^3, \lambda^4, \lambda^5)$$
$$= \mathrm{diag}(u_n, u_n, u_n, u_n + c, u_n - c) \tag{11}$$

where u_n is the projection of the velocity vector on the normal to the boundary, c is the sound velocity, and L is the matrix of the left eigenvectors.

Then, the temporal evolutions of the primitive variables ($\boldsymbol{\delta V'}$) and those of the characteristic variables are linked by

$$\boldsymbol{\delta W'} = L\boldsymbol{\delta V'}, \qquad \boldsymbol{\delta V'} = L^{-1}\boldsymbol{\delta W'} \tag{12}$$

where $\boldsymbol{W'}$ is the vector of the characteristic variables.

We can now derive a nonreflecting boundary condition for the fluctuating field following Thomson[23]:

$$\frac{\partial W^{1,2}}{\partial t} \equiv \boldsymbol{\delta W}^{1,2} = \begin{cases} 0 & \text{if} \quad \lambda_i \le 0 \\ \dfrac{W^{1,2\,n+1} - W^{1,2n}}{\Delta t} & \text{if} \quad \lambda_i > 0 \end{cases} \tag{13}$$

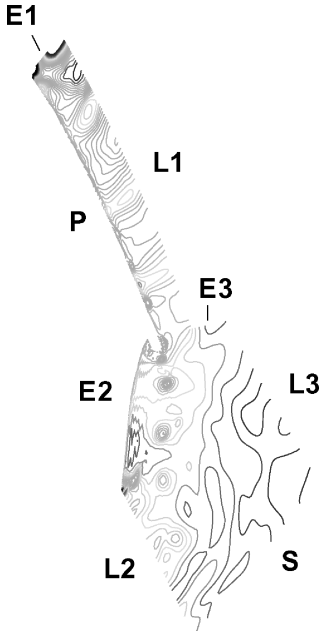

Fig. 16 Isovalues of the density field, reflecting inflow condition.

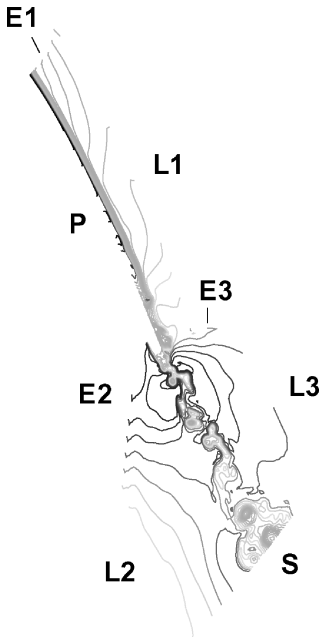

Fig. 17 Isovalues of the density field, nonreflecting inflow condition.

D. Results

The preceding boundary condition is used on the inflow boundaries of the NLDE domain and is compared to a simple boundary condition, which consists of a zeroth-order extrapolation. The results can be found in Figs. 16 (zeroth-order extrapolation) and 17 (nonreflecting boundary condition).

In these two figures, the isovalues of the density are represented. It is observed that with the zeroth-order extrapolation pressure waves pile up, leading to unreliable results, whereas with the nonreflecting boundary conditions pressure waves are correctly leaving the NLDE domain leading to a locally LES-like solution.

This example shows that in some case the acoustic response of the inflow boundary condition can be more important than the prescription of a realistic inflow velocity field. This remark can be limited to inflow domain beginning in the laminar or transitional part of the boundary layer, but it can have a wide range of applications in particular for turbomachinery.

VII. Conclusions

The problem of inflow turbulent conditions for LES has been addressed through three examples that are representative of this issue

recently treated at ONERA. First, the performance of an extension to compressible flows of the rescaling method of Lund et al.[3] has been assessed. The accuracy of the method is proven by comparisons with experimental data. Such a precision in the definition of the inflow condition is not always necessary because in the case of the deep cavity the imposition of turbulent fluctuations has nearly no influence on the accuracy of the simulation on this acoustically driven flow. The third case demonstrates that particular attention must be paid to the response of the inflow condition to acoustic perturbations, which have more importance than the prescription of a realistic velocity field when the beginning of the domain is located on a laminar/transitional part of a boundary layer.

References

[1]Sagaut, P., *Large-Eddy Simulation for Incompressible Flows*, 2nd ed., Springer-Verlag, Berlin, 2002.

[2]Druault, P., Lardeau, S., Bonnet, J.-P., Coiffet, F., Delville, J., Lamballais, E., Largeau, J.-F., and Perret, L., "Generation of Three-Dimensional Inlet Conditions for Large-Eddy Simulation," *AIAA Journal*, Vol. 42, No. 3, 2004, pp. 447–456.

[3]Lund, T. S., Wu, X., and Squire, K. D., "Generation of Turbulent Inflow Data for Spatially-Developing Boundary Layer Simulations," *Journal of Computational Physics*, Vol. 140, No. 2, 1998, pp. 233–258.

[4]Urbin, G., and Knight, D., "Large-Eddy Simulation of a Supersonic Boundary Layer Using an Unstructured Grid," *AIAA Journal*, Vol. 39, No. 7, 2001, pp. 1288–1295.

[5]Stolz, S., and Adams, N. A., "LES of Supersonic Boundary Layers Using the Approximate Deconvolution Model," *Direct and Large-Eddy Simulation—IV*, Kluwer Academic, Norwell, MA, 2001, pp. 269–276.

[6]Schröder, W., Meinke, M., Ewert, R., and El-Askary, W., "LES of a Turbulent Flow Around a Sharp Trailing Edge," *Direct and Large-Eddy Simulation—IV*, Kluwer Academic, Norwell, MA, 2001, pp. 353–363.

[7]Deleuze, J., "Structure d'une Couche Limite Turbulente Soumise à Une Onde de Choc Incidente," Ph.D. Dissertation, Univ. Aix-Marseille II, Marseille, France, Sept. 1995.

[8]Laurent, H., "Turbulence d'Une Interaction Onde de Choc/Couche Limite sur Une Paroi Adiabatique ou Chauffée," Ph.D. Dissertation, Univ. Aix-Marseille II, Marseille, France, May 1996.

[9]Garnier, E., Sagaut, P., and Deville, M., "Large-Eddy Simulation of Shock/Bounadary Layer Interaction," *AIAA Journal*, Vol. 40, No. 10, 2002, pp. 1935–1944.

[10]Lenormand, E., Sagaut, P., Phuoc, L. T., and Comte, P., "Subgrid-Scale Models for Large-Eddy Simulation of Compressible Wall Bounded Flows," *AIAA Journal*, Vol. 38, No. 8, 2000, pp. 1340–1350.

[11]Rai, M., Gatski, T., and Erlebacher, G., "Direct Simulation of Spatially Evolving Compressible Turbulent Boundary Layers," AIAA Paper 95-0583, Jan. 1995.

[12]Spyropoulos, E. T., and Blaisdell, G. A., "Large-Eddy Simulation of a Spatially Evolving Supersonic Turbulent Boundary-Layer Flow," *AIAA Journal*, Vol. 36, No. 11, 1998, pp. 1983–1990.

[13]Eléna, M., and Lacharme, J.-P., "Experimental Study of a Supersonic Turbulent Boundary Layer Using a Laser Doppler Anemometer," *Journal de Mécanique Théorique et Appliquée*, Vol. 7, No. 2, 1988, pp. 175–190.

[14]Forestier, N., Jacquin, L., and Geffroy, P., "The Mixing Layer over a Deep Cavity at High-Subsonic Speed," *Journal of Fluid Mechanics*, Vol. 475, 2003, pp. 101–145.

[15]Larchevêque, L., Sagaut, P., Mary, I., Labbé, O., and Comte, P., "Large-Eddy Simulation of a Compressible Flow past a Deep Cavity," *Physics of Fluids*, Vol. 15, No. 1, 2003, pp. 193–210.

[16]Mary, I., and Sagaut, P., "LES of a Flow Around an Airfoil near Stall," *AIAA Journal*, Vol. 40, No. 6, 2002, pp. 1139–1145.

[17]Morris, P. J., Long, N. L., Bangalore, A., and Wang, Q., "A Parallel Three-Dimensional Computational Aeroacoustics Method Using Nonlinear Disturbance Equations," *Journal of Computational Physics*, Vol. 133, 1997, pp. 56–74.

[18]Labourasse, E., and Sagaut, P., "Reconstruction of Turbulent Fluctuations Using a Hybrid RANS/LES Approach," *Journal of Computational Physics*, Vol. 182, Oct. 2002, pp. 301–336.

[19]Raverdy, B., Mary, I., Sagaut, P., and Liamis, N., "High-Resolution Large-Eddy Simulation of the Flow Around a Low-Pressure Turbine Blade," *AIAA Journal* (to be published).

[20]Spalart, P. R., and Almaras, S. R., "A One-Equation Turbulence Model for Aerodynamic Flows," *La Recherche Aérospatiale*, Vol. 1, 1994, pp. 5–21.

[21]Hirsch, C., *Numerical Computation of Internal and External Flow*, Wiley, New York, 1990, Chap. 3.

[22]Poinsot, T. J., and Lele, S. K., "Boundary Conditions for Direct Simulations of Compressible Viscous Flows," *Journal of Computational Physics*, Vol. 101, 1991, pp. 104–129.

[23]Thomson, K. W., "Time Dependent Boundary Conditions for Hyperbolic Systems II," *Journal of Computational Physics*, Vol. 89, 1990, pp. 439–461.

F. Grinstein
Guest Editor